

This is a repository copy of *Huge power factor in p-type half-Heusler alloys NbFeSb and TaFeSb*.

White Rose Research Online URL for this paper:

<https://eprints.whiterose.ac.uk/id/eprint/145918/>

Version: Accepted Version

---

**Article:**

Naydenov, Genadi Antonov, Hasnip, Philip James orcid.org/0000-0002-4314-4093, Probert, Matthew Ian James orcid.org/0000-0002-1130-9316 et al. (1 more author) (2019) Huge power factor in p-type half-Heusler alloys NbFeSb and TaFeSb. *Journal of physics : Materials*. 035002.

<https://doi.org/10.1088/2515-7639/ab16fb>

---

**Reuse**

This article is distributed under the terms of the Creative Commons Attribution (CC BY) licence. This licence allows you to distribute, remix, tweak, and build upon the work, even commercially, as long as you credit the authors for the original work. More information and the full terms of the licence here:

<https://creativecommons.org/licenses/>

**Takedown**

If you consider content in White Rose Research Online to be in breach of UK law, please notify us by emailing [eprints@whiterose.ac.uk](mailto:eprints@whiterose.ac.uk) including the URL of the record and the reason for the withdrawal request.

ACCEPTED MANUSCRIPT • OPEN ACCESS

## Huge power factor in p-type half-Heusler alloys NbFeSb and TaFeSb

To cite this article before publication: Genadi Naydenov *et al* 2019 *J. Phys. Mater.* in press <https://doi.org/10.1088/2515-7639/ab16fb>

### Manuscript version: Accepted Manuscript

Accepted Manuscript is “the version of the article accepted for publication including all changes made as a result of the peer review process, and which may also include the addition to the article by IOP Publishing of a header, an article ID, a cover sheet and/or an ‘Accepted Manuscript’ watermark, but excluding any other editing, typesetting or other changes made by IOP Publishing and/or its licensors”

This Accepted Manuscript is © 2019 The Author(s). Published by IOP Publishing Ltd.

As the Version of Record of this article is going to be / has been published on a gold open access basis under a CC BY 3.0 licence, this Accepted Manuscript is available for reuse under a CC BY 3.0 licence immediately.

Everyone is permitted to use all or part of the original content in this article, provided that they adhere to all the terms of the licence <https://creativecommons.org/licenses/by/3.0>

Although reasonable endeavours have been taken to obtain all necessary permissions from third parties to include their copyrighted content within this article, their full citation and copyright line may not be present in this Accepted Manuscript version. Before using any content from this article, please refer to the Version of Record on IOPscience once published for full citation and copyright details, as permissions may be required. All third party content is fully copyright protected and is not published on a gold open access basis under a CC BY licence, unless that is specifically stated in the figure caption in the Version of Record.

View the [article online](#) for updates and enhancements.

# Huge power factor in p-type half-Heusler alloys NbFeSb and TaFeSb

G. A. Naydenov,\* P. J. Hasnip, V. K. Lazarov, and M. I. J. Probert  
*Department of Physics, University of York, York YO10 5DD, United Kingdom*  
 (Dated: March 13, 2019)

NbFeSb is a promising thermoelectric material which according to experimental and theoretical studies exhibits a high power factor of up to 10 mW/(m·K<sup>2</sup>) at room temperature and  $ZT$  of 1 at 1000 K. In all previous theoretical studies,  $\kappa_{latt}$  is calculated using simplified models, which ignore structural defects. In this work, we calculate  $\kappa_{latt}$  by solving the Boltzmann Transport Equation and subsequently including the contributions of grain boundaries, point defects and electron-phonon interaction. The results for  $\kappa_{latt}$  and  $ZT$  are in excellent agreement with experimental measurements. In addition, we investigate theoretically the thermoelectric properties of TaFeSb. The material has recently been synthesised experimentally, thus confirming the theoretical hypothesis for its stability. This encourages a full-scale computation of its thermoelectric performance. Our results show that TaFeSb is indeed an excellent thermoelectric material which has a very high power factor of 16 mW/(m·K<sup>2</sup>) at room temperature and  $ZT$  of 1.5 at 1000 K.

## I. INTRODUCTION

NbFeSb is a half-Heusler intermetallic compound which has recently attracted a lot of attention as a potential thermoelectric material due to its ecologically friendly properties and the relatively high earth abundance of Nb and Fe. NbFeSb alloys are reported to have a large power factor of up to 10 mW/(m·K<sup>2</sup>) [1], beating some of the best thermoelectrics, e.g. Bi<sub>2</sub>Te<sub>3</sub>. However, their thermal conductivity is also a lot higher than Bi<sub>2</sub>Te<sub>3</sub> [1–3]. The high thermal conductivity of NbFeSb is phonon dominated and this provides much room for improvement of the current thermoelectric figure of merit maximum of  $ZT=1$  at 1000K.

The thermoelectric figure of merit is given by the equation  $ZT = S^2\sigma T/\kappa$  and several theoretical and experimental studies which aim to optimise the thermal conductivity ( $\kappa$ ) as well as the Seebeck coefficient ( $S$ ) and electrical conductivity ( $\sigma$ ) have been conducted in the past couple of years [1, 2, 4–10]. This optimisation is done by  $p$ -type doping with Ti, Hf and Zr for Nb or Sn for Sb. Such an approach maximises the power factor by fine tuning of the doping levels and decreases the lattice thermal conductivity by enhancing the phonon scattering due to the mass difference between the dopant and host atoms. To date, the best NbFeSb results are obtained by Ti-doping [1] due to the large mass difference between Ti and Nb. The mass difference can be further enhanced if Nb is substituted with a heavier but chemically similar element like Ta, which is something that has not yet been thoroughly investigated.

The first aim of this study is to compute the lattice thermal conductivity ( $\kappa_{latt}$ ) of NbFeSb using the semi-classical Boltzmann Transport Equation (BTE) and compare the obtained theoretical thermoelectric (TE) results to experimental measurements. The second aim is to use the same approach and calculate the TE properties of a

compound very similar to NbFeSb, namely TaFeSb. A theoretical study by Bhattacharya and Madsen [9] reports that TaFeSb is a stable compound which can also be doped with Ti in a similar way to NbFeSb. A very recent experimental study by Zhu *et al.* [11] investigates extensively the phase stability of the compound and provides an XRD pattern after the successful experimental synthesis of TaFeSb. The main interest in TaFeSb comes from the fact that it has the same number of valence electrons as NbFeSb, while Ta has almost twice the mass of Nb. This suggests that TaFeSb should have the same good electronic TE properties as NbFeSb. In addition, the heavier Ta should also lead to an increase in the scattering strength in doped TaFeSb due to point defects and thus decrease  $\kappa_{latt}$ . As a result, TaFeSb may be expected to have a significantly higher  $ZT$  than NbFeSb but until now there have been no full-scale theoretical studies on the pure TaFeSb compound to confirm this hypothesis. Zeeshan *et al.* [12] investigates the thermoelectric properties of TaFeSb but without computing the electron relaxation time or including the additional phonon scattering mechanisms. Another recent study conducted by Yu *et al.* [8] investigates the effect of Ta but in NbFeSb systems. Hence, this is clearly a very hot topic and there is a strong need for a full study of the thermoelectric properties of TaFeSb.

## II. METHODOLOGY AND THEORY

We split our calculations into two stages. We solve the electron BTE in the first stage and the phonon BTE in the second one. The energy distribution of the charge carriers and phonons is computed from first-principles.

### A. DFT calculations and electronic TE properties

The first-principles calculations were performed with the CASTEP[13] code and the generalized gradient approximation Perdew–Burke–Ernzerhof (GGA-PBE)

\* email: gan503@york.ac.uk

exchange-correlation functional [14]. On-the-fly ultrasoft pseudopotentials (C9 set)[15] were used with a plane-wave cut-off energy of 700 eV with a grid scale of size 2.0. A cubic unit cell, corresponding to four elementary rhombohedral cells, was used for all simulations. The Brillouin zone was sampled using a MonkhorstPack grid[16] with an  $8 \times 8 \times 8$   $\vec{k}$ -points mesh (equivalent to  $\vec{k}$ -points spacing of  $0.021\ 2\pi\text{\AA}^{-1}$ ). The structure was fully optimized until pressure and energy were converged to 0.1 GPa and 0.02 meV/atom, respectively. Density of states (DOS) and partial density of states (PDOS) were analysed using the OptaDOS code[17].

Electronic transport properties were calculated using the semi-classical Boltzmann transport formalism as implemented in the BoltzTraP code [18]. The electronic eigenenergies required for the transport properties were calculated with CASTEP on a  $48 \times 48 \times 48$   $\vec{k}$ -points mesh, which was later interpolated on a 5 times denser mesh in BoltzTraP. The simulated half-Heusler alloys are isotropic and the Seebeck coefficient  $S$ , electrical conductivity  $\sigma$  and electron thermal conductivity  $\kappa_{el}$  can be evaluated as the average of the trace of the respective tensors. The final results are obtained as a function of the temperature ( $T$ ) for 37 fixed doping levels from  $n_h = 10^{18}\text{ cm}^{-3}$  to  $n_h = 10^{22}\text{ cm}^{-3}$ . BoltzTraP calculates both electrical and electron thermal conductivity as  $\sigma/\tau$  and  $\kappa_{el}/\tau$  where  $\tau$  is the relaxation time. We use the deformation potential (DP) theory to compute  $\tau$  [19]. A more detailed explanation of the steps needed for calculating  $\tau$  is provided in the supplementary materials.

## B. Lattice thermal conductivity modelling

### 1. ShengBTE and thirdorder programs

The lattice thermal conductivity was calculated by solving the phonon BTE in ShengBTE, which as inputs requires the second order force constants (usually just called the ‘force constants’) and the anharmonicity (third order force constants) of the system. The second order force constants were obtained with CASTEP using density-functional perturbation theory (DFPT) for the phonons [20]. The calculations used the GGA-PBE exchange-correlation functional[14], on-the-fly norm-conserving pseudopotentials (NCP17 set) and a plane-wave cut-off energy of 2000 eV with a grid scale of size 2.0. The Brillouin zone was sampled using a MonkhorstPack[16] grid with an  $5 \times 5 \times 5$   $\vec{k}$ -points mesh (equivalent to  $\vec{k}$ -points spacing of  $0.034\ 2\pi\text{\AA}^{-1}$ ). A  $\vec{q}$ -point grid of the same size and spacing was used for calculating the second order force constants.

The third order force constants were calculated using the finite-displacement supercell approach. The set of supercells and the reconstruction of the force constants was performed by the *thirdorder.py* script that is provided as part of the ShengBTE package. The *ab initio*

calculations were done using CASTEP. The settings for these runs included: a  $2 \times 2 \times 2$  cubic supercell, on-the-fly ultrasoft pseudopotentials (C9 set), a plane-wave cut-off energy of 600 eV with a grid scale of size 2.0 and a very fine energy per atom convergence tolerance of  $2 \times 10^{-10}$  eV.

ShengBTE computes the intrinsic lattice thermal conductivity  $\kappa_{int}$  due to 3P (three-phonon) processes. We have also included the effect of GB (grain boundaries), PD (point defects) and EP (electron-phonon) interaction to the lattice thermal conductivity. More details on how this is done are given in the supplementary materials.

## III. RESULTS

The results are split into two subsections. The first one presents the calculations on the TE properties of NbFeSb. We start by following the well-established procedure of using BoltzTraP [18] to obtain the electronic properties of the material and then solve the phonon BTE using ShengBTE. [21] Furthermore, we build upon the method proposed by Hong *et al.*[5] for the inclusion of point defects and introduce the contributions of grain boundaries and electron-phonon interaction to the lattice thermal conductivity of NbFeSb. To the best of our knowledge, this is the first instance when the lattice thermal conductivity of NbFeSb is calculated by solving the BTE and including all these additional contributions. For this reason, the results are thoroughly compared to the available experimental data. The second section follows a similar layout but is focused on TaFeSb and the observed improvements in TE properties with respect to NbFeSb.

It is worth pointing out that BoltzTraP calculates the TE properties at different doping levels by changing the chemical potential implicitly and hence the dopant atoms are not explicitly included. For this reason, the *p*-type compounds in electronic properties section are referred simply as NbFeSb and TaFeSb. However, the computation of the change in the lattice thermal conductivity due to point defects requires knowledge of the atomic mass of the dopant atoms. In this case, the structures are referred as  $\text{Nb}_{1-x}\text{Ti}_x\text{FeSb}$  and  $\text{Ta}_{1-x}\text{Ti}_x\text{FeSb}$ , with Ti being used for the *p*-type doping.

### A. NbFeSb

#### 1. Electronic structure

NbFeSb is a half-Heusler compound, which has a composition of XYZ, where X and Y are transition metals and Z is a main group element. The crystal structure is face-centred cubic, having space group  $F\bar{4}3m$  (216). The lattice constant is calculated to be 5.96 Å, which agrees well with the experimental value of 5.95 Å [4]. The band structure and density of states (DOS) are presented in

Fig. 1. The figure shows that the conduction band minimum (CBM) is at the  $\Gamma$ -point, whereas the valence band maximum (VBM) is positioned at the L-point. The magnitude of the formed indirect band gap ( $\epsilon_g$ ) is 0.53 eV, which is in an excellent agreement with other theoretical [1, 5, 6] ( $\epsilon_g = 0.52$  and 0.53 eV) and experimental [1] ( $\epsilon_g = 0.51$  eV) studies. The partial DOS show that Fe and Nb are the main contributors to states around the Fermi level. This means that the power factor is mainly affected by Fe and Nb rather than Sb.

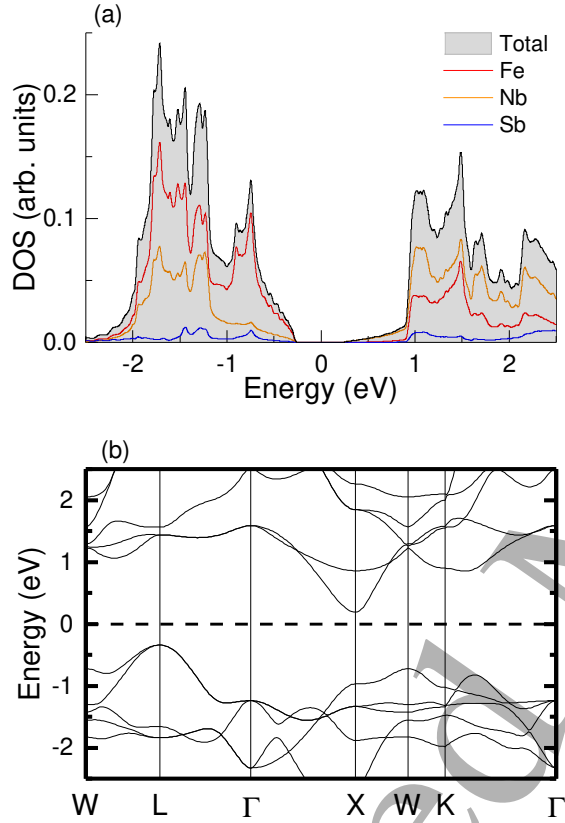


Figure 1. Density of states (a) and band structure (b) graphs of NbFeSb.

## 2. Electronic TE properties

The parameters needed to calculate the electron relaxation time for bulk NbFeSb are given in Table I. These include the deformation potential ( $V_{DP}$ ), effective mass of the charge carriers ( $m^*$ ), carrier mobility ( $\mu$ ) and relaxation time ( $\tau$ ). The elastic constants are given in Table S1 in the supplementary materials. The values of the parameters obtained for holes are slightly higher, but within the margin of error, than the ones obtained experimentally by He *et al.*[1] and Fu *et al.*[4]. The experimental measurements have been performed on doped systems

which exhibit structural defects. Therefore, a slight overestimate is to be expected when the results are compared to the modelled perfect bulk system. To the best of our knowledge there are no experimental results on the electron parameters. However, the electron values presented in Table I agree extremely well with the theoretical prediction of Hong *et al.*[5]. The magnitude of the deformation potential constant for holes ( $V_{DP} = -13.98$  eV) is lower than the one for electrons ( $V_{DP} = -14.53$  eV). This can be explained by the different dispersion of the valence and conduction bands. The bottom conduction band is more dispersive than the top valence band, and the applied strain has a smaller effect on the flatter bands. Due to the difference in the dispersion of the bands, the effective mass of electrons  $m_{el}^* = 0.35(m_e)$  is much smaller than that of the holes  $m_h^* = 1.65(m_e)$ . This results in a much lower mobility ( $\mu_h = 28.02 \text{ cm}^2\text{V}^{-1}\text{s}^{-1}$ ) of the heavier holes and a lower relaxation time of  $\tau_h = 26.23$  fs at 300 K. This value of the relaxation time, with the included temperature dependence of  $\tau \propto 1/T^{3/2}$  is used to post-process the results obtained from BoltzTraP for the *p*-type behaviour of NbFeSb.

Table I. Parameters needed for electron and hole  $\tau$  calculations of NbFeSb. These include the deformation potential ( $V_{DP}$ ), effective mass of charge carriers ( $m^*$ ), carrier mobility ( $\mu$ ) and relaxation time ( $\tau$ ) at 300 K for electrons and holes.

Carrier type	$V_{DP}$ (eV)	$m^*$ ( $m_e$ )	$\mu$ ( $\text{cm}^2\text{V}^{-1}\text{s}^{-1}$ )	$\tau$ (fs)
holes	-13.98	1.65	28.02	26.23
electrons	-14.53	0.35	1243.93	247.54

The calculated thermoelectric properties of *p*-type NbFeSb are shown in Fig. 2. All quantities agree very well with results obtained in the other theoretical studies [5, 6]. It can be seen that the Seebeck coefficient (top left graph) reaches values up of 700  $\mu\text{V/K}$  at low temperature (around 300 K) and at extremely small doping levels (between 0.04 and 0.004% hole concentration). When the doping concentration is increased to the experimental values of  $x = 0.04$  ( $n_h = 8 \times 10^{20}\text{cm}^{-3}$ ) the Seebeck coefficient becomes 129  $\mu\text{V/K}$  and 266  $\mu\text{V/K}$  at 300 K and 1000 K, respectively. These values are slightly lower than the experimental results obtained by Fu *et al.* [4] ( $S = 150 \mu\text{V/K}$  and 285  $\mu\text{V/K}$  at 300 K and 1000 K, respectively) and He *et al.*[1] ( $S = 175$  and 300  $\mu\text{V/K}$  at 300 and 1000 K, respectively). It is worth mentioning, however, that a lower doping level in the theoretical model of  $n_h = 6 \times 10^{20}\text{cm}^{-3}$  ( $x = 0.03$ ) yields identical results to the experimental ones obtained for  $x = 0.04$  by Fu *et al.*[4]. This could mean that an  $x = 0.04$  does not strictly correspond to  $8 \times 10^{20}\text{cm}^{-3}$  hole concentration in the experimental samples, and some of the holes could be compensated. In fact, Fu *et al.*[4] results show that a doping level of  $x = 0.04$  corresponds more to  $n_h = 6 \times 10^{20}\text{cm}^{-3}$  rather than  $n_h = 8 \times 10^{20}\text{cm}^{-3}$ , as the theory suggests. For simplicity, however, we use the theoretical relation between  $x$  and  $n_h$  ( $\text{volume} = x/n_h$ ), where the volume

is theoretically calculated to be  $52.86 \times 10^{-24} \text{cm}^3$ .

The electrical conductivity  $\sigma$  and electronic thermal conductivity  $\kappa_{el}$  also agree very well with other theoretical studies[5, 6], but are slightly larger than found in experiment [1, 4]. There are a few reasons for this discrepancy. As already mentioned, the carrier mobility of the perfect crystal is expected to be higher than  $\mu$  of the doped compounds, hence  $\tau$  and  $\sigma$  are also larger. Second, the temperature dependence of  $\tau$  is no longer proportional to  $T^{-3/2}$  at temperature  $< 450$  K[1, 4]. Finally, the constant relaxation time approximation lacks dependence on the chemical potential, which means that additional scattering events are not captured when the doping levels are increased. Thus,  $\sigma$  and  $\kappa_{el}$  tend to be overestimated at high doping levels. Nevertheless, the current model for  $\tau$  is a computationally inexpensive approach that allows us to calculate values for  $\sigma$  and  $\kappa_{el}$ , which agree relatively well with both theoretical and experimental studies.

The highest value of the power factor  $PF = S^2\sigma$  is obtained at  $n_h = 7 \times 10^{20} \text{cm}^{-3}$  ( $x = 0.037$ ) and yields  $PF = 9.15$  and  $5.23 \text{ mW}/(\text{m}\cdot\text{K}^2)$  at 300 K and 1000 K, respectively. This result is very close to the key result of He *et al.*[1] study of  $PF = 10.6 \text{ mW}/(\text{m}\cdot\text{K}^2)$  at room temperature and  $x \approx 0.05$ . In general, the power factor values remain consistent with the experimental measurements up to  $n_h = 2 \times 10^{21} \text{cm}^{-3}$  ( $x = 0.1$ ). Beyond that value, the theoretical prediction starts to overestimate the experimental results by values up to  $\approx 2 \text{ mW}/(\text{m}\cdot\text{K}^2)$  when one reaches  $x = 0.3$ . Such behaviour is also noticed by the other theoretical studies mentioned before. The reason for this could be either the constant relaxation time approximation, or the fact that the heavy doping significantly changes the electronic structure of the system. However, as shown experimentally, NbFeSb exhibits its best thermoelectric performance at around  $x = 0.05$ , and this region is accurately modelled by the current theoretical approach.

### 3. Lattice thermal conductivity

The phonon density of states (DOS) are presented in Fig. 3. The data is in a good agreement with the results obtained by Hong *et al.* [5] and Zeeshan *et al.* [12] and as there are no imaginary frequencies the structure is mechanically stable. The phonon DOS can be split into three regions. The first one is at low frequency,  $\omega < 170 \text{ cm}^{-1}$  where the lattice vibrations are primarily due to Sb atoms. The dominant contributor to the phonon DOS for  $170 < \omega < 230 \text{ cm}^{-1}$  is Nb, whereas for  $\omega > 230 \text{ cm}^{-1}$  lattice vibrations are predominantly due to Fe with a small contribution from Nb. The Nb atomic vibrations have the biggest frequency spread among the constituents of the material. In addition, the mass difference between Nb and the dopant atoms (here assumed to be Ti) leads to an increase in the scattering strength. Thus, the lattice thermal conductivity  $\kappa_{latt}$  of NbFeSb

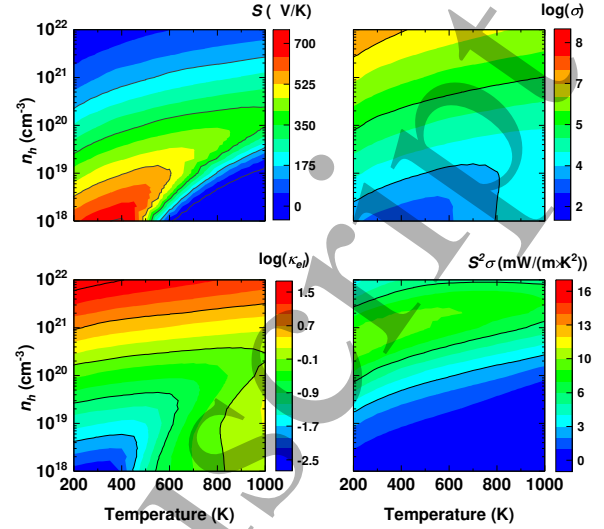


Figure 2. Colour maps of the electronic TE properties of *p*-type NbFeSb. The magnitude of the electrical conductivity  $\sigma$  (top right) and electronic thermal conductivity  $\kappa_{el}$  (bottom left) is given on a log scale. A maximum power factor (bottom right) value of  $PF = S^2\sigma = 9.15 \text{ mW}/(\text{m}\cdot\text{K}^2)$  is obtained at 300 K and  $n_h = 7 \times 10^{20} \text{cm}^{-3}$  ( $x = 0.037$ ).

can be reduced significantly by doping. Our results show the clear presence of a phonon gap at  $\omega \approx 275 \text{ cm}^{-1}$ , something which is not observed either by Hong *et al.* or Zeeshan *et al.*[12]. The reason for this discrepancy comes from the choice of the  $\vec{q}$ -point grid for the phonon calculations. The phonon DOS converges slowly and the gap only becomes apparent when the  $\vec{q}$ -point mesh is at least  $3 \times 3 \times 3$  or equivalently a spacing of  $0.056 \text{ } 2\pi \text{ \AA}^{-1}$ .

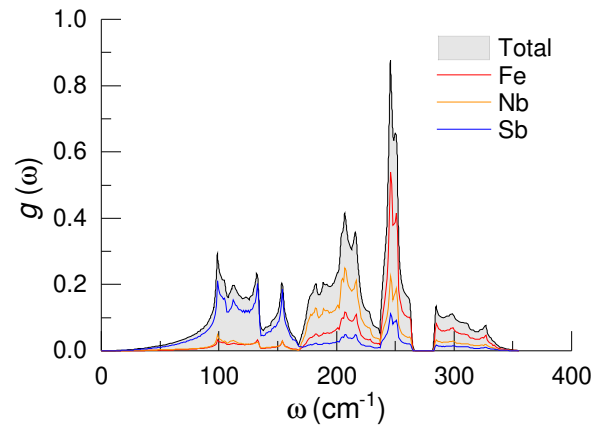


Figure 3. Phonon density of states of NbFeSb.

Next we focus on the estimated value for the lattice thermal conductivity and how different contributions affect it. The intrinsic value of  $\kappa_{latt}$  obtained from Sheng-BTE is  $21.82$  and  $6.49 \text{ Wm}^{-1}\text{K}^{-1}$  at 300 and 1000 K,



respectively. This agrees very well with the theoretical result obtained by Hong *et al.* [5] but is a bit higher than the experimental measurements [1, 4]. The main reasons for this discrepancy is the fact that there are no defects such as grain boundaries, point defects or dopant atoms in the modelled structure. To correct this, we include the effect of all mentioned impurities by using Klemens' model[22] and calculating the impact on the intrinsic value obtained from ShengBTE.

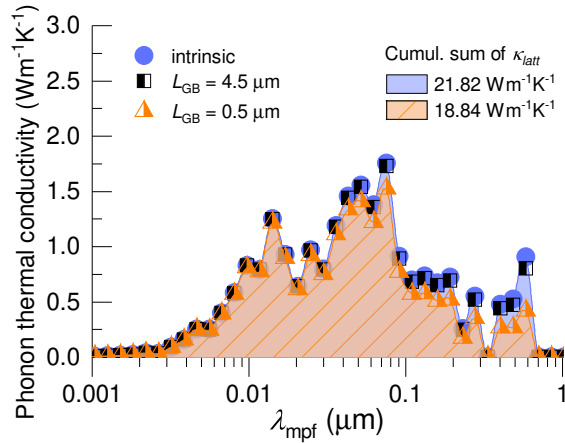


Figure 4. The impact of grain boundaries on the lattice thermal conductivity of NbFeSb at 300 K.

The study conducted by He *et al.* reports that the size of the grain boundaries in NbFeSb varies between 0.3 and 4.5  $\mu\text{m}$ , depending on the hot pressing temperature. Figure 4 shows how the lattice thermal conductivity of phonons with a given mean free path changes at room temperature when grain boundaries are included in the theoretical model. The graph illustrates the effect of grain boundaries ( $L_{\text{GB}}$ ) by considering two different average sizes of  $L_{\text{GB}} = 4.5$  and 0.5  $\mu\text{m}$ . Blue circles represent the intrinsic values of  $\kappa_{\text{latt}}$  and it can be seen that  $L_{\text{GB}} = 4.5$   $\mu\text{m}$ , illustrated with black and white squares, have an almost negligible impact on  $\kappa_{\text{latt}}$ . However, there is a noticeable change in  $\kappa_{\text{latt}}$  when the size of the grain boundaries is reduced to 0.5  $\mu\text{m}$  (orange triangles), and the accumulated value of  $\kappa_{\text{latt}}$  becomes 18.84  $\text{Wm}^{-1}\text{K}^{-1}$ . For completeness,  $L_{\text{GB}} = 0.3$   $\mu\text{m}$  was also tested and yielded a result of  $\kappa_{\text{latt}} = 17.59$   $\text{Wm}^{-1}\text{K}^{-1}$  at 300 K. Both results for  $L_{\text{GB}} = 0.3$  and 0.5  $\mu\text{m}$  are within the margin of error of the experimental value of  $\kappa_{\text{latt}} \approx 17$   $\text{Wm}^{-1}\text{K}^{-1}$  (undoped NbFeSb, 12% relative error).

To complete the calculation, we include the effect of point defects and electron-phonon interaction to  $\kappa_{\text{latt}}$ . The computation of the electron-phonon interaction requires knowledge of the electron  $\tau$ . The lack of doping level dependence in the constant relaxation time approximation makes it unsuitable for calculating the electron-phonon contribution. The experimental data from the He *et al.* study, including the temperature and doping dependencies, was used in accordance to the theoretical

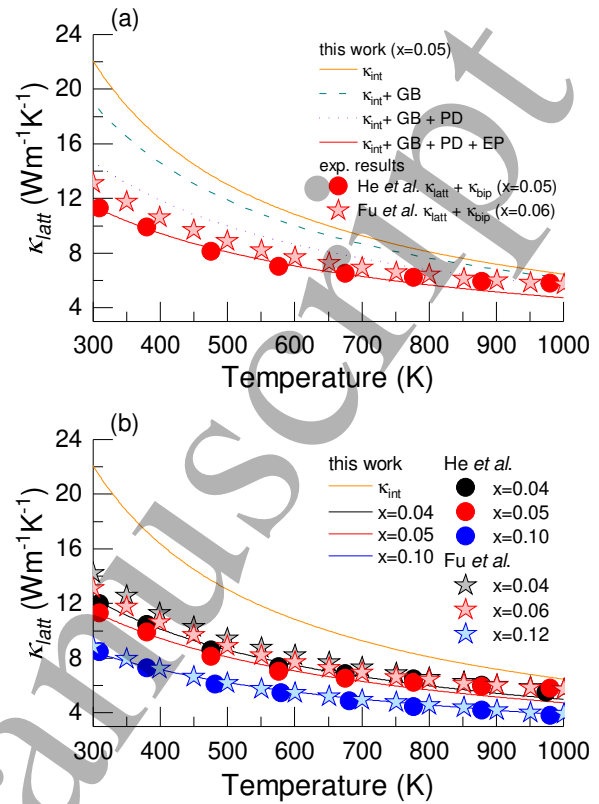


Figure 5. Figure (a) shows the contribution of grain boundaries GB, point defects PD and electron-phonon interaction EP to the lattice thermal conductivity  $\kappa_{\text{int}}$  of NbFeSb. Figure (b) compares the theoretical prediction of this study (solid lines) for  $\text{Nb}_{1-x}\text{Ti}_x\text{FeSb}$  with  $L_{\text{GB}} = 0.5$   $\mu\text{m}$  to the experimental results (stars and circles).

model and is discussed in more details in the supplementary materials. Figure 5(a) shows how the lattice thermal conductivity of  $\text{Nb}_{1-x}\text{Ti}_x\text{FeSb}$  is reduced when all contributions are included. The results are presented for doping  $x = 0.05$  and the best match to the experimental data is obtained with  $L_{\text{GB}} = 0.5$   $\mu\text{m}$ . Figure 5(b) compares  $\kappa_{\text{latt}}$  when all contributions have been added to the experimental results. The computed values for the lattice thermal conductivity agree very well with the experimental study, particularly with the He *et al.* study at temperature up to 700 K. There is a slight underestimate of the theoretical value of  $\kappa_{\text{latt}}$  at higher temperature for  $x=0.04$  and  $x=0.05$ . This can be explained with the lack of a bipolar thermal conductivity ( $\kappa_{\text{bip}}$ ) term in the calculations. In order to compute that, one needs to calculate a value for the electron relaxation time which depends on the doping level. Therefore, using the constant relaxation time approximation to compute  $\kappa_{\text{bip}}$  would yield inaccurate results. However, as it can be seen in Figure 5(b), the contribution of  $\kappa_{\text{bip}}$  is sufficiently small that the computed values are still in a good agreement with the experimental measurements.

#### 4. Figure of merit

The final results on the thermoelectric figure of merit  $ZT$  for the  $p$ -type  $\text{Nb}_{1-x}\text{Ti}_x\text{FeSb}$  are presented in Fig. 6. A comparison between  $ZT$  values obtained in this study and the experimental data is shown in Figure 6(a). There is a good agreement up to  $T = 650$  K between our results and the measurements conducted by He *et al.* The overestimate of  $ZT$  above this temperature for  $x = 0.04$  and  $0.05$  can be explained by the missing  $\kappa_{bip}$  term in the lattice thermal conductivity. This has already been discussed in the previous section and explains why the agreement between the experimental and theoretical results at high temperatures improves with the increase of the doping concentration. Additionally, the limitations of the constant relaxation time approximation, e.g. no dependence on the chemical potential and no inclusion of the extrinsic scattering mechanisms, can easily add up and lead to the observed discrepancies at lower temperatures. The results in this study slightly overestimate  $ZT$  when compared to Fu *et al.*[4] However, as with the lattice thermal conductivity results, there is a mismatch between the experimental results presented by He *et al.* and Fu *et al.* The latter uses a much lower annealing temperature, and so the density of the grain boundaries in the sample is expected to be higher. This further confirms that the constant relaxation time approximation could play a major role along with the bipolar term in the discrepancy between the theoretical and experimental results. The sample preparation in the Fu *et al.* study influences both the electrical and thermal conductivity, and as a consequence, the measured  $ZT$  values are expected to be a bit lower than the ones obtained in our calculations.

The colour map in Fig. 6(b) shows that  $\text{NbFeSb}$  remains most efficient at high temperature, despite the big power factor of  $PF = 9.3 \text{ mW}/(\text{m}\cdot\text{K}^2)$  at 300 K. The  $p$ -doped  $\text{NbFeSb}$  displays its best figure of merit ( $ZT \approx 1.0$ ) at  $T = 1000$  K and high doping levels between  $x = 0.05$  and  $0.10$ , corresponding to  $n_h = 1 \times 10^{21}$  and  $2 \times 10^{21} \text{ cm}^{-3}$ . This result is typical for half-Heusler alloys[23] and illustrates that a reduction of  $\kappa_{latt}$  can significantly enhance the thermoelectric performance of similar half-Heusler alloys.

### B. TaFeSb

#### 1. Electronic structure

The crystal structure of  $\text{TaFeSb}$  is very similar to  $\text{NbFeSb}$  with the only difference being the atomic species on the X-site. The lattice constant is calculated to be  $5.95 \text{ \AA}$ . The band structure and density of states (DOS) are presented in Fig. 7. The band gap of  $\text{TaFeSb}$  is calculated to be  $0.86 \text{ eV}$ , close to the value  $\epsilon_g = 0.93 \text{ eV}$  computed by Bhattacharya and Madsen[9]. It can be seen that the valence bands and DOS near the Fermi level re-

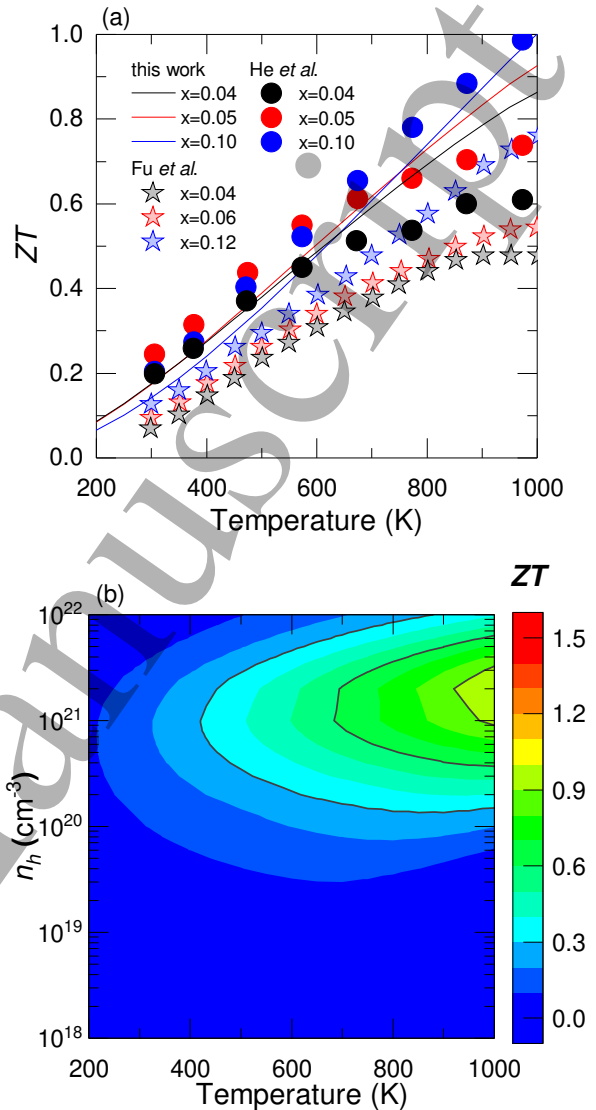


Figure 6. Comparison between our theoretical results and experimental measurements on  $p$ -type  $\text{NbFeSb}$  at  $x = 0.04$ ,  $0.05$  and  $0.10$  (a). Subfigure (b) is a colour map which shows the  $ZT$  of  $p$ -type  $\text{NbFeSb}$  with respect to the charge carrier concentration and temperature, with a maximum  $ZT$  of 1 at  $n_h = 2 \times 10^{21} \text{ cm}^{-3}$  ( $x=0.1$ ) and  $T = 1000 \text{ K}$ .

main almost unchanged when compared to  $\text{NbFeSb}$ . This suggests that the  $p$ -type  $S$ ,  $\sigma$  and  $\kappa_{el}$  should exhibit the same behaviour as in  $\text{NbFeSb}$ , leaving the relaxation time as the determining factor for any change in the electronic TE properties.

#### 2. Electronic TE properties

The relaxation time along with the parameters necessary for its calculation are shown in Table II. There is a noticeable reduction in the deformation potential values



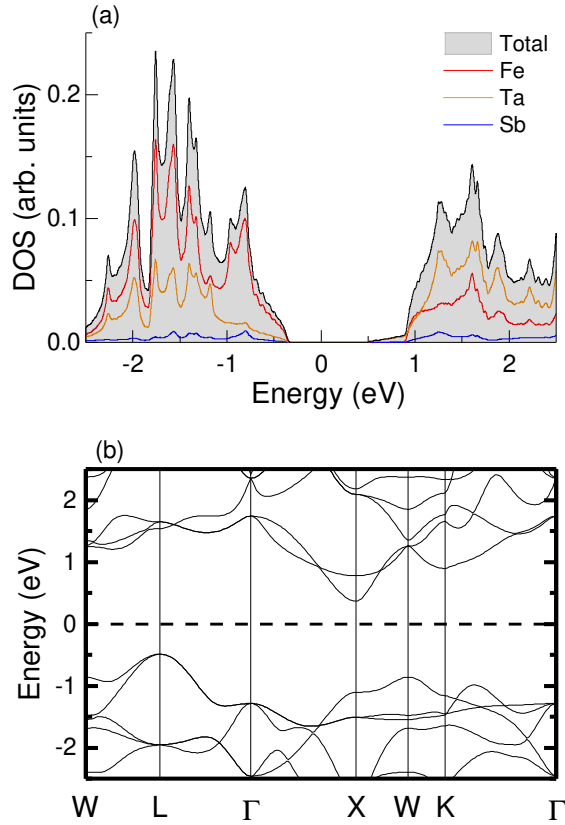


Figure 7. Density of states (a) and band structure (b) graphs of TaFeSb.

for both holes  $V_{DP} = -11.06$  eV ( $-13.98$  eV for NbFeSb) and electrons  $V_{DP} = -11.81$  eV ( $-14.53$  eV for NbFeSb). This means that stress has less effect on the electronic structure of TaFeSb. In addition, a slight reduction in the effective mass is also observed, with  $m_h^* = 1.57(m_e)$ . As a result, the mobility of the holes and relaxation time are increased to  $\mu_h = 53.11 \text{ cm}^2\text{V}^{-1}\text{s}^{-1}$  and  $\tau_h = 47.32$  fs.

Table II. Parameters needed for electron and hole  $\tau$  calculations of TaFeSb. These include the deformation potential constant ( $V_{DP}$ ), effective mass of charge carriers ( $m^*$ ), carrier mobility ( $\mu$ ) and relaxation time ( $\tau$ ) at 300 K for electrons and holes.

Carrier type	$V_{DP}$ (eV)	$m^*$ ( $m_e$ )	$\mu$ ( $\text{cm}^2\text{V}^{-1}\text{s}^{-1}$ )	$\tau$ (fs)
holes	-11.06	1.57	53.11	47.32
electrons	-11.81	0.38	1629.74	350.26

Next we present the electronic TE properties of TaFeSb in the form of colour maps in Fig. 8. The colour maps investigate a very wide doping and temperature range and might not be intuitive for comparison purposes. For that reason, we also provide 2D plots in Fig. 9, which compare the electronic properties of TaFeSb and NbFeSb for

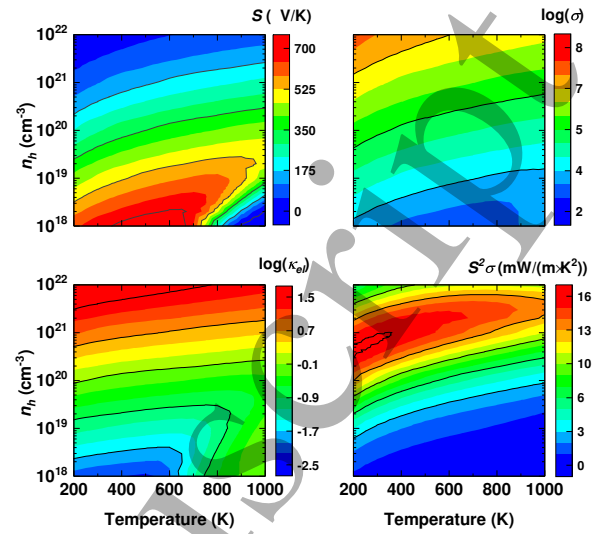


Figure 8. Colour maps of the electronic TE properties of *p*-type TaFeSb. The magnitude of the electrical conductivity  $\sigma$  (top right) and electronic thermal conductivity  $\kappa_{el}$  (bottom left) is given on a log scale. A maximum power factor (bottom right) value of  $PF = S^2\sigma = 16.11 \text{ mW}/(\text{m}\cdot\text{K}^2)$  is obtained at 300 K and  $n_h = 7 \times 10^{20} \text{ cm}^{-3}$  ( $x = 0.037$ ).

the common doping levels of  $x = 0.04$ ,  $0.05$  and  $0.10$ . The value of the *p*-type Seebeck coefficient for  $x=0.05$  is calculated to be  $113.81$  and  $247.5 \mu\text{V}/\text{K}$  at 300 and 1000 K, respectively. The change in  $S$  with respect to the NbFeSb results for the same doping concentration is less than 1%, which is expected due to the similarity in the valence bands of both materials. On the other hand, the bigger band gap in TaFeSb results in a bigger *p*-type  $S$  at a very low doping concentration and temperature around 600 K. This is visualised with an increase of the red area in Fig. 8(a) when compared to NbFeSb in Fig. 2(a). The results confirm that not only does TaFeSb exhibit a competitive Seebeck coefficient around the experimentally investigated doping levels, but also shows a significant improvement at very low  $n_h$  and moderate  $T$ .

The results obtained from BoltzTraP for  $\sigma$  and  $\kappa_{el}$  predict a behaviour analogous to the changes observed for *p*-type  $S$ . Therefore, the increase of  $\tau$  (holes), which is  $\approx 80\%$ , yields a significant improvement in  $\sigma$ , and an increase in  $\kappa_{el}$ . The increase of  $\sigma$  leads to an astonishing power factor of  $PF \approx 16 \text{ mW}/(\text{m}\cdot\text{K}^2)$  at room temperature and  $x=0.03$ - $0.05$ . For comparison, the power factor of NbFeSb is estimated to be  $9$ - $10 \text{ mW}/(\text{m}\cdot\text{K}^2)$ , and the maximum value for  $\text{Fe}_2\text{VAl}$  is measured to be  $5.5 \text{ mW}/(\text{m}\cdot\text{K}^2)$  [24]. The compounds based on the already established TE material  $\text{Bi}_2\text{Te}_3$  have a power factor between  $1.5$  and  $6 \text{ mW}/(\text{m}\cdot\text{K}^2)$  [3, 25, 26]. The improvement in  $PF$  of TaFeSb over NbFeSb is maintained over a wide range of doping levels from  $n_h = 10^{20} \text{ cm}^{-3}$  to  $n_h = 2 \times 10^{21} \text{ cm}^{-3}$  and at higher temperatures (compare

Fig. 8(d) and Fig. 2(d) and note the unchanged ranges). In summary, TaFeSb has a significantly better electronic TE performance than NbFeSb due to the increased band gap and higher mobility of the charge carriers.

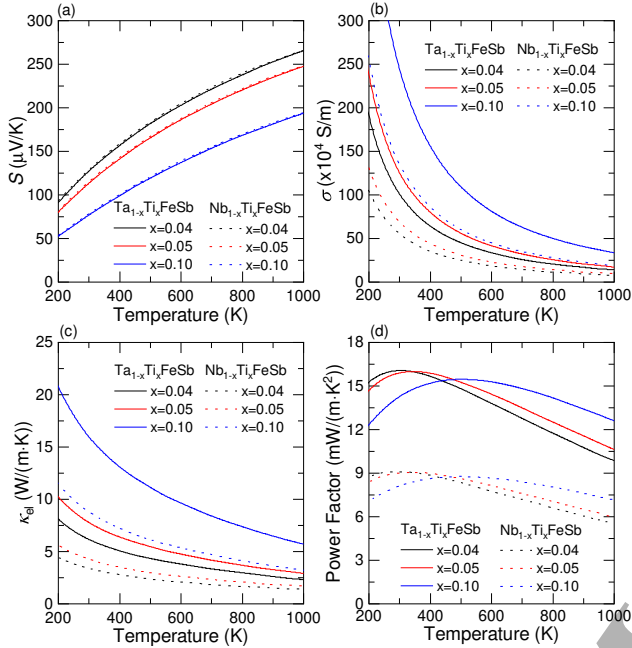


Figure 9. Comparison of the thermoelectric properties of TaFeSb and NbFeSb for  $x = 0.04, 0.05$  and  $0.10$ . The subfigures compare the Seebeck coefficient (a), electrical conductivity (b), electronic thermal conductivity (c), and power factor (d).

### 3. Lattice thermal conductivity

The phonon density of states of TaFeSb, presented in Fig. 10, show a close resemblance to the NbFeSb results. There are no imaginary frequencies and so this structure is also mechanically stable. The data is again in a very good agreement with the results obtained by Zeeshan *et al.* [12] The low frequency region is up to  $150 \text{ cm}^{-1}$  and is dominated by Sb. The intermediate region between  $150$  and  $220 \text{ cm}^{-1}$  is due to Ta, instead of Nb. The last region is dominated by Fe atomic vibrations and occupies the high frequencies up to  $350 \text{ cm}^{-1}$ . It is also noticeable that a gap is formed in between the regions dominated by Ta and Fe. Our calculations show that the intrinsic value of  $\kappa_{latt}$  is  $20.57$  and  $5.75 \text{ Wm}^{-1}\text{K}^{-1}$  at  $300$  and  $1000 \text{ K}$ , respectively. This is slightly lower than the NbFeSb results and can be accounted for by the gap between Ta and Fe in Fig. 10.

The effect of grain boundaries on  $\kappa_{latt}$  of TaFeSb at  $300 \text{ K}$  is shown in Fig. 11. Grain boundaries of size  $4.5 \mu\text{m}$  have an almost negligible effect on the lattice thermal conductivity. When their size is reduced to  $0.5 \mu\text{m}$   $\kappa_{latt}$  is computed to be  $17.63 \text{ Wm}^{-1}\text{K}^{-1}$ . Although a

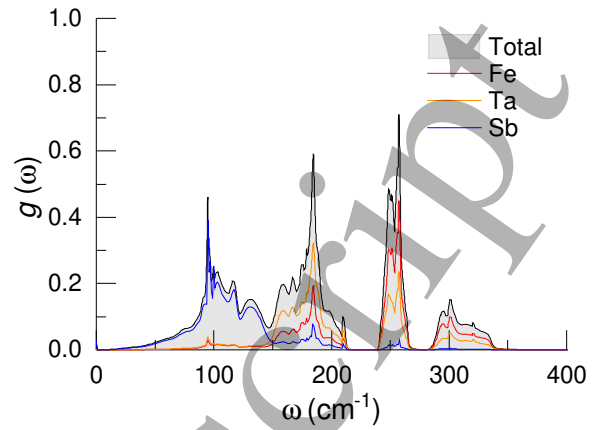


Figure 10. Phonon density of states of TaFeSb.

similar behaviour was noticed in NbFeSb, the presence of an additional gap in the phonon DOS of TaFeSb leads to a different phonon mean free path  $\lambda_{mfp}$  distribution. A common dip in the phonon thermal conductivity is observed for both TaFeSb and NbFeSb between  $0.3$  and  $0.4 \mu\text{m}$ . This can be explained by the common gap in the phonon DOS at  $\omega \approx 275 \text{ cm}^{-1}$ . However, whilst the Ta-Fe gap in TaFeSb leads to an extra dip at  $0.08 \mu\text{m}$ , this has a small effect as phonons with  $\lambda_{mfp}$  less than  $0.3 \mu\text{m}$  contribute less to the total lattice thermal conductivity. Despite this difference, grain boundaries of the same size seem to reduce  $\kappa_{latt}$  in both TaFeSb and NbFeSb by a similar amount. This means that the change in the phonon mean free path distribution has an effect only on the intrinsic value of  $\kappa_{latt}$  but little impact on the effect of grain boundaries.

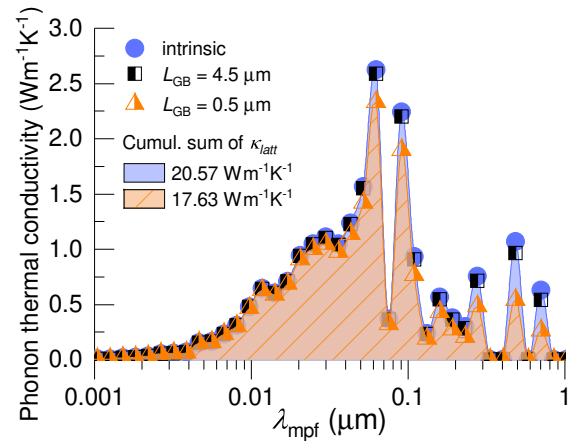


Figure 11. The impact of grain boundaries on the lattice thermal conductivity of TaFeSb at  $300 \text{ K}$ .

Next we proceed by adding the contribution of the point defects due to Ti doping. The major difference between TaFeSb and NbFeSb is in the atomic mass of the X element. The mass of Ta is  $180.95 \text{ amu}$ , whereas Nb is

significantly lighter with a mass of 92.906 amu. One of the crucial parameters in the Klemens model[22] for the thermal conductivity of systems with point defects is the mass difference between the dopant atom (Ti) and the atoms which are substituted (Ta or Nb): a larger mass difference results in a greater reduction in the lattice thermal conductivity. Therefore, the lattice thermal conductivity of  $\text{Ta}_{1-x}\text{Ti}_x\text{FeSb}$  is expected to be affected significantly by the Ti dopants. Fig. 12(a) illustrates this point by comparing the  $\text{Ta}_{1-x}\text{Ti}_x\text{FeSb}$  and  $\text{Nb}_{1-x}\text{Ti}_x\text{FeSb}$  results. It is indeed seen that the reduction in  $\kappa_{latt}$  of the Ta-based compound due to point defects (Ti doping) is much more significant. For  $\text{Nb}_{1-x}\text{Ti}_x\text{FeSb}$  the lattice thermal conductivity is reduced by 23% and 9% at 300 K and 1000 K, respectively, when the point defects are included. For  $\text{Ta}_{1-x}\text{Ti}_x\text{FeSb}$  these numbers increase to 37% and 18% at 300 K and 1000 K, respectively.

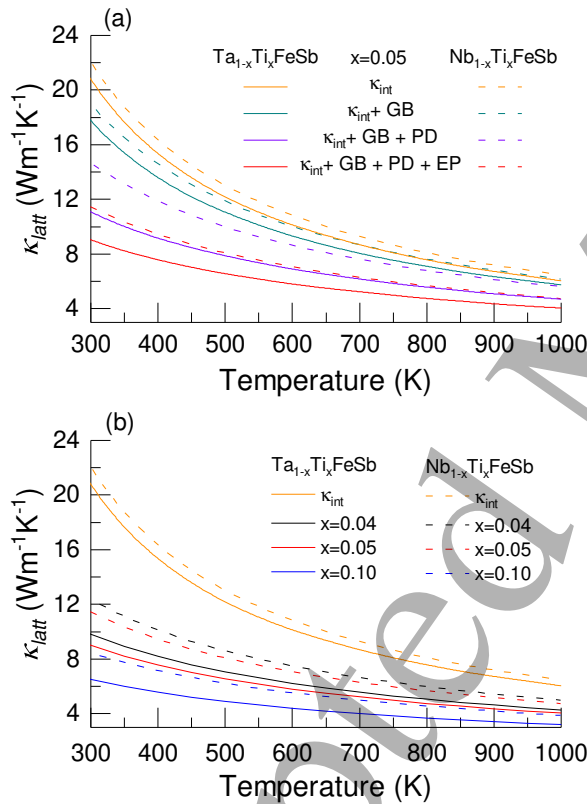


Figure 12. Figure (a) compares the lattice thermal conductivity of  $\text{Ta}_{1-x}\text{Ti}_x\text{FeSb}$  (solid lines) and  $\text{Nb}_{1-x}\text{Ti}_x\text{FeSb}$  (dashed lines) when the contribution of grain boundaries GB, point defects PD and electron-phonon interaction EP are added. The biggest change occurs when the contribution from point defects is added to the Ta-based compound. Figure (b) compares  $\kappa_{latt}$  with all contributions included at different doping levels.

The last contribution which needs to be added is the electron-phonon interaction. As already described, it is meaningless to use the constant relaxation time approximation to compute the electron-phonon interaction. For

that reason, experimental data was used earlier to obtain a value for the NbFeSb compound. Unfortunately, there are no experimental measurements which can be used to extract a value for the electron-phonon contribution in TaFeSb. For practical purposes and because of the similarity in the electronic structure and phonon DOS between TaFeSb and NbFeSb, we will use the electron-phonon contribution which was extracted for NbFeSb. In the worst case, such an approximation would lead to an overestimate of  $\kappa_{latt}$  and an underestimate of the  $ZT$  of TaFeSb rather than the opposite.

Fig. 12(b) shows the lattice thermal conductivity of  $\text{Ta}_{1-x}\text{Ti}_x\text{FeSb}$  and  $\text{Nb}_{1-x}\text{Ti}_x\text{FeSb}$  at different doping levels with all contributions included. The trend shows that  $\kappa_{latt}$  of the Ta-based compound is lower at all doping levels. At  $x=0.05$ ,  $\kappa_{latt}$  is lower by 21% ( $\kappa_{latt}=8.99 \text{ Wm}^{-1}\text{K}^{-1}$ ) and 15% ( $\kappa_{latt}=4.04 \text{ Wm}^{-1}\text{K}^{-1}$ ) at 300 K and 1000 K, respectively. At  $x=0.10$ , the reduction is 23% ( $\kappa_{latt}=8.43 \text{ Wm}^{-1}\text{K}^{-1}$ ) and 18% ( $\kappa_{latt}=3.20 \text{ Wm}^{-1}\text{K}^{-1}$ ) at 300 K and 1000 K, respectively. The improvement of 15-23%, as already discussed, comes from the slightly lower intrinsic value of  $\kappa_{latt}$  for TaFeSb and the bigger mass difference between Ta and Ti. There is also a noticeable similarity of the lattice thermal conductivity of  $\text{Ta}_{1-x}\text{Ti}_x\text{FeSb}$  at  $x=0.05$  and that of  $\text{Nb}_{1-x}\text{Ti}_x\text{FeSb}$  at  $x=0.10$ . This hints that TaFeSb might require less doping than NbFeSb to reach its maximum  $ZT$  value.

### C. Comparison between $ZT$ of $p$ -type TaFeSb and NbFeSb

Finally, we present the results on  $ZT$  of  $\text{Ta}_{1-x}\text{Ti}_x\text{FeSb}$  and compare them to the  $\text{Nb}_{1-x}\text{Ti}_x\text{FeSb}$  results. Fig. 13 shows that the maximum thermoelectric figure of merit is obtained at  $T=1000 \text{ K}$ ,  $x=0.05$  and is equal to  $ZT=1.53$ . For comparison the maximum  $ZT$  value for  $\text{Nb}_{1-x}\text{Ti}_x\text{FeSb}$  is only 1.01, and at  $x=0.10$ . Fig. 13(a) shows that  $\text{Ta}_{1-x}\text{Ti}_x\text{FeSb}$  exhibits higher  $ZT$  across the entire temperature range and at all doping levels. The main difference to  $\text{Nb}_{1-x}\text{Ti}_x\text{FeSb}$  is that there is a 50% increase in  $ZT$  and that the peak is achieved at  $x=0.05$  rather than  $x=0.10$ , which is in agreement with the prediction made in the lattice thermal conductivity section.

The colour map in Fig. 13(b) reveals a broad area between 800 and 1000 K, and  $x=0.02$  and  $x=0.15$  in which the  $ZT$  of  $\text{Ta}_{1-x}\text{Ti}_x\text{FeSb}$  is higher than 1.2. At moderate temperature (500-700 K) the  $ZT$  value drops to  $\approx 1$ , which is still considered as an excellent TE result. Even at room temperature, the TE figure of merit ( $ZT=0.3$ ) is almost 2 times bigger than that of NbFeSb ( $ZT=0.17$ ). The wide range of conditions, which result in a good  $ZT$  value, suggests that  $p$ -type TaFeSb can indeed be used as a novel material for efficient thermoelectric devices.

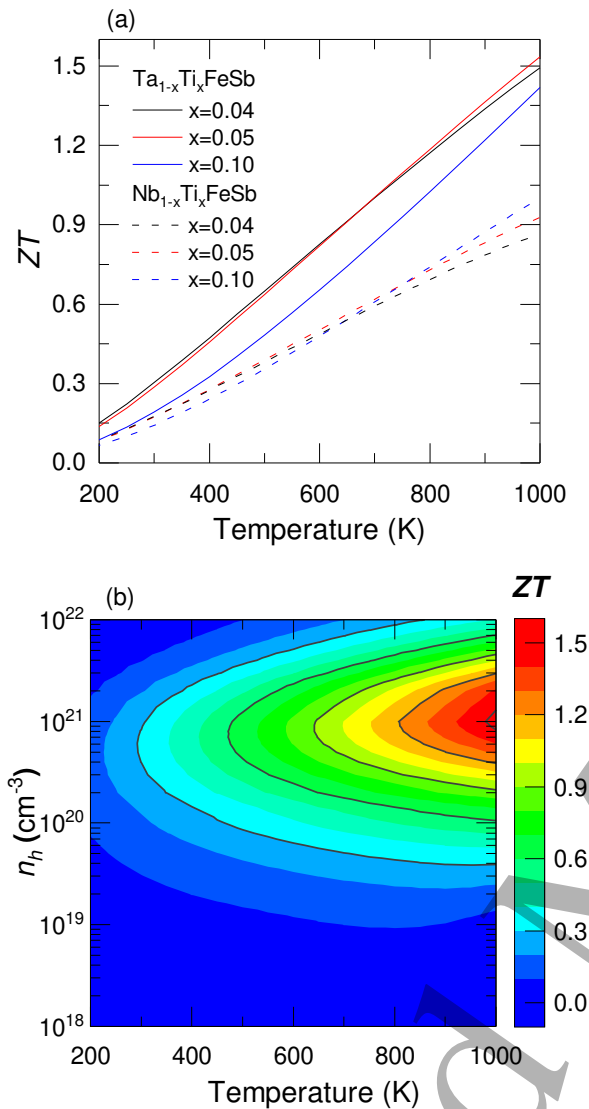


Figure 13. Comparison between  $p$ -type TaFeSb and NbFeSb at  $x = 0.04, 0.05$  and  $0.10$  (a). Subfigure (b) is a colour map which shows the  $ZT$  of  $p$ -type TaFeSb with respect to the charge carrier concentration and temperature, with a maximum  $ZT$  of 1.53 at  $n_h = 1 \times 10^{21} \text{ cm}^{-3}$  ( $x=0.05$ ) and  $T = 1000 \text{ K}$ .

#### IV. CONCLUSIONS

We have conducted a thorough study of the thermoelectric properties of  $p$ -type NbFeSb and TaFeSb. In addition to solving the Boltzmann transport equations for electrons and phonon with *ab initio* inputs, several approximations were also included in the process. These are the constant relaxation time approximation with no

dependence on the chemical potential due to doping, the choice of grain boundary size and the inclusion of the electron-phonon interaction based on experimental data. This multi-step procedure needs to be executed with caution, and so at each step the results have been thoroughly compared to the available experimental measurements. We would like to point out that although the results in this study look promising and are consistent with the expectations, one should not use the presented theoretical framework lightly on fully unknown compounds. The key feature of this study was to preserve the chemical environment of NbFeSb and change it slightly to TaFeSb in a way that the empirical Klemens' equation is still applicable.

In summary, the NbFeSb results agree extremely well with multiple theoretical and experimental studies. The same procedure was then used to perform a full-scale computation on the TE properties of TaFeSb. The results have shown that both compounds exhibit high power factor at room temperature and have a good thermoelectric figure of merit at high temperatures. At 1000 K we find  $PF = 9 \text{ mW}/(\text{m}\cdot\text{K}^2)$  and  $ZT = 1$  for NbFeSb and  $PF = 16 \text{ mW}/(\text{m}\cdot\text{K}^2)$  and  $ZT = 1.5$  for TaFeSb. The higher atomic mass of Ta (compared to Nb) increases the scattering strength in Ti-doped TaFeSb, which reduces the lattice thermal conductivity of the compound. At the same time,  $p$ -type charge carries in TaFeSb exhibit higher mobility and relaxation time, which increases the power factor. The net result is a material with an amazing net power factor of  $16 \text{ mW}/(\text{m}\cdot\text{K}^2)$  and  $ZT$  value which is approximately 50% better than that of NbFeSb.

In conclusion, TaFeSb not only appears to be a better TE material than NbFeSb, but it also opens a new path of TE optimisation of materials based on the two alloys. In theory, an alloy based on  $\text{Nb}_{1-x}\text{Ta}_x\text{FeSb}$  should exhibit good electrical properties due to the similarities in the electronic structure of NbFeSb and TaFeSb. At the same time, the mass difference between Nb and Ta should create additional scattering centres which would suppress the lattice thermal conductivity even before doping, and so the final doped compound should exhibit an even higher  $ZT$  value. This is further hinted by a very recent experimental study by Yu *et al.*[8], which reports the successful synthesis of  $\text{Nb}_{1-x}\text{Ta}_x\text{FeSb}$  alloys and a measured  $ZT$  of up to 1.6.

#### ACKNOWLEDGEMENTS

PJH acknowledges financial support from EPSRC (grant ref. EP/R025770/1). We are grateful for computational support from the UK national high performance computing service, ARCHER, for which access was obtained via the UKCP consortium and funded by EPSRC grant ref. EP/P022561/1.

[1] R. He, D. Kraemer, J. Mao, L. Zeng, Q. Jie, Y. Lan, C. Li, J. Shuai, H. S. Kim, Y. Liu, D. Broido, C.-W. Chu, G. Chen, and Z. Ren, *Proceedings of the National Academy of Sciences of the United States of America* **113**, 13576 (2016).

[2] A. Tavassoli, F. Failamani, A. Grytsiv, G. Rogl, P. Heinrich, H. Müller, E. Bauer, M. Zehetbauer, and P. Rogl, *Acta materialia* **135**, 263 (2017).

[3] F. Wu, W. Wang, X. Hu, and M. Tang, *Progress in Natural Science: Materials International* **27**, 203 (2017).

[4] C. Fu, T. Zhu, Y. Liu, H. Xie, and X. Zhao, *Energy & environmental science* **8**, 216 (2014).

[5] A. J. Hong, L. Li, R. He, J. J. Gong, Z. B. Yan, K. F. Wang, J.-M. Liu, and Z. F. Ren, *Scientific reports* **6**, 22778 (2016).

[6] T. Fang, S. Zheng, H. Chen, H. Cheng, L. Wang, and P. Zhang, *RSC advances* **6**, 10507 (2016).

[7] T. Fang, S. Zheng, T. Zhou, L. Yan, and P. Zhang, *Physical chemistry chemical physics: PCCP* **19**, 4411 (2017).

[8] J. Yu, C. Fu, Y. Liu, K. Xia, U. Aydemir, T. C. Chasapis, G. J. Snyder, X. Zhao, and T. Zhu, *Advanced Energy Materials* **8** (2018), 10.1002/aenm.201701313.

[9] S. Bhattacharya and G. K. H. Madsen, *J. Mater. Chem. C* **4**, 11261 (2016).

[10] X. Zhang, Y. Wang, Y. Yan, C. Wang, G. Zhang, Z. Cheng, F. Ren, H. Deng, and J. Zhang, *Scientific reports* **6**, 33120 (2016).

[11] H. Zhu, J. Mao, Y. Li, J. Sun, Y. Wang, Q. Zhu, G. Li, Q. Song, J. Zhou, Y. Fu, R. He, T. Tong, Z. Liu, W. Ren, L. You, Z. Wang, J. Luo, A. Sotnikov, J. Bao, K. Nielsch, G. Chen, D. J. Singh, and Z. Ren, *Nature communications* **10**, 270 (2019).

[12] M. Zeeshan, T. Nautiyal, J. van den Brink, and H. C. Kandpal, *Physical Review Materials* **2**, 065407 (2018).

[13] S. J. Clark, M. D. Segall, C. J. Pickard, P. J. Hasnip, M. I. J. Probert, K. Refson, and M. C. Payne, *Zeitschrift für Kristallographie - Crystalline Materials* **220**, 567 (2005).

[14] J. P. Perdew, K. Burke, and M. Ernzerhof, *Physical review letters* **77**, 3865 (1996).

[15] K. Lejaeghere *et al.*, *Science* **351**, aad3000 (2016).

[16] H. J. Monkhorst and J. D. Pack, *Physical review. B, Condensed matter* **13**, 5188 (1976).

[17] A. J. Morris, R. J. Nicholls, C. J. Pickard, and J. R. Yates, *Computer physics communications* **185**, 1477 (2014).

[18] G. K. H. Madsen and D. J. Singh, *Computer physics communications* **175**, 67 (2006).

[19] J. Bardeen and W. Shockley, *Physical Review* **80**, 72 (1950).

[20] K. Refson, P. R. Tulip, and S. J. Clark, *Physical review. B, Condensed matter* **73**, 155114 (2006).

[21] W. Li, J. Carrete, N. A. Katcho, and N. Mingo, *Comp. Phys. Commun.* **185**, 17471758 (2014).

[22] F. L. Madarasz and P. G. Klemens, *International journal of thermophysics* **8**, 257 (1987).

[23] M. Rull-Bravo, A. Moure, J. F. Fernández, and M. Martín-González, *RSC advances* **5**, 41653 (2015).

[24] Y. Nishino, *IOP Conference Series: Materials Science and Engineering* **18**, 142001 (2011).

[25] J.-H. Kim, J.-Y. Choi, J.-M. Bae, M.-Y. Kim, and T.-S. Oh, *Materials Transactions* **54**, 618 (2013).

[26] S. V. Ovsyannikov, V. V. Shchennikov, G. V. Vorontsov, A. Y. Manakov, A. Y. Likhacheva, and V. A. Kulbachinskii, *Journal of applied physics* **104**, 053713 (2008).

[27] F. VanGessel, J. Peng, and P. W. Chung, *Journal of Materials Science* **53**, 5641 (2018).

[28] G. A. Slack, *The Journal of physics and chemistry of solids* **34**, 321 (1973).

[29] T. Jia, G. Chen, and Y. Zhang, *Physical review. B, Condensed matter* **95**, 155206 (2017).

[30] F. Giustino, M. L. Cohen, and S. G. Louie, *Physical review. B, Condensed matter* **76**, 165108 (2007).

[31] A. Fonari and C. Sutton, "Effective mass calculator," <https://github.com/afonari/emc> (2012).

[32] P. G. Klemens, *International journal of thermophysics* **22**, 265 (2001).

[33] J. Callaway, *Physical Review* **113**, 1046 (1959).

[34] X. Shi, Y. Pei, G. Jeffrey Snyder, and L. Chen, *Energy & environmental science* **4**, 4086 (2011).

[35] J. Yang, D. T. Morelli, G. P. Meisner, W. Chen, J. S. Dyck, and C. Uher, *Physical Review B: Condensed Matter and Materials Physics* **65** (2002), 10.1103/PhysRevB.65.094115.



# Supplemental Materials: Computation of the thermoelectric properties of NbFeSb and TaFeSb

## V. THEORETICAL APPROACH

The usual theoretical approach is to split the thermoelectric calculations into two stages. The first stage solves the semi-classical Boltzmann Transport Equation (BTE) for electrons which requires knowledge of the electron density of states (DOS) of the material. The DOS can be easily calculated using first principles electronic structure programs. The BTE for electrons in the constant relaxation time ( $\tau$ ) approximation is found using the computed DOS and the BoltzTraP program[22]. The output of BoltzTraP includes the electronic conductivity  $\sigma$  and the electron thermal conductivity  $\kappa_{el}$  as a function of the electron relaxation time  $\tau$ . The choice of  $\tau$  is usually arbitrary but Hong *et al.* [5] showed that for NbFeSb a computationally inexpensive approach based upon deformation potential theory [19] can be used to obtain reasonable results for  $\tau$ .

The second stage is to calculate the phonon contribution to the thermal conductivity ( $\kappa_{latt}$ ) which is more computationally demanding. There are several different approaches which can be used to obtain  $\kappa_{latt}$ . These include (i) calculating the phonon DOS and using the Boltzmann Transport Equations for phonons, [27] (ii) assuming an arbitrary value for  $\kappa_{latt}$  [9], (iii) calculating a theoretical minimum of  $\kappa_{latt}$  for a given compound [6] and (iv) obtaining  $\kappa_{latt}$  via Slack's equation [28], which requires knowledge of the anharmonicity of the system (Grüneisen parameter  $\gamma$ ) and the Debye temperature ( $\theta_D$ ). The last two parameters can be calculated either via the bulk and shear moduli[29] or via the quasi-harmonic approximation as shown in the Hong *et al.* study [5]. The main advantage of the last three approaches is that they are not computationally intensive and provide a rough estimate of  $\kappa_{latt}$ , which allows the user to obtain a reasonable estimate for  $ZT$ . The drawback, however, is that the phonon contribution to  $\kappa$  is derived indirectly via either the elastic constants, or by considering only the acoustic phonons. Hence such results neglect the details of the geometry and chemical structure of the material and can often be inaccurate [29]. To the best of our knowledge a full-scale computation of  $\kappa_{latt}$  of NbFeSb using the phonon DOS and the anharmonic force constants has not been published before. In this study, the ShengBTE program [21] is used to solve the BTE for phonons. In addition, to the intrinsic value of  $\kappa_{latt}$  obtained from ShengBTE, we add the contributions from grain boundaries, point defects and electron-phonon interaction

### A. Computing electron relaxation time

As mentioned in the manuscript, BoltzTraP actually calculates both  $\sigma/\tau$  and  $\kappa_{el}/\tau$  where  $\tau$  is the relaxation time. An evaluation of  $\tau$  could be done either with the electron-phonon interaction using Wannier functions (EPW method)[30] or via the deformation potential (DP) theory[19]. While the EPW method is the more sophisticated approach, it can be prohibitively expensive for more complicated systems and still does not take into account the role of point defects and grain boundaries. Although DP theory lacks dependence on the chemical potential, it is a lot quicker and has been reported to predict a reasonable value for  $\tau$  of NbFeSb[5]. Therefore, a value for  $\tau$  was obtained using the following DP formulae [19]:

$$\mu = \frac{2\sqrt{2}\pi e\hbar^4 c_{11}}{3(k_B T)^{3/2} m^{*5/2} V_{DP}} \quad (S1)$$

$$\tau = \frac{\mu m^*}{e} \quad (S2)$$

where  $\mu$  is the mobility of the charge carriers,  $e$  is the charge of an electron,  $\hbar$  is the reduced Planck's constant,  $c_{11}$  is one of the three independent elastic constant,  $k_B$  is the Boltzmann constant, and  $V_{DP}$  is the DP constant which is calculated using:

$$V_{DP} = \frac{dE_{edge}}{d\alpha}, \quad \alpha = \frac{a - a_0}{a_0} \quad (S3)$$

where  $E_{edge}$  is the energy at the valence band maximum (VBM) or conduction band minimum (CBM),  $\alpha$  is the uniaxial strain along the direction of the lattice vector  $a$ . The strain is defined by varying  $a$  with respect to the calculated equilibrium lattice constant  $a_0$ .

The effective mass  $m^*$ , which is used in Eqn. S1 and S2 is obtained with the 'Effective Mass Calculator for Semiconductors' (EMC) [31]. The effective mass is calculated exactly at the VBM and CBM and is defined as:



$$\left(\frac{1}{m^*}\right)_{ij} = \frac{1}{\hbar^2} \frac{\partial^2 E_{edge}(\vec{k})}{\partial k_i \partial k_j}, \quad i, j = x, y, z \quad (S4)$$

The heavy hole (hh) and light hole (lh) band yield a different characteristic relaxation time. However, from Eqn. S1 and S2 it can be seen that  $\tau \propto 1/m^{*3/2}$  and different contributions to the relaxation time are summed by Matthiessen's rule. Therefore, a weighted effective mass of the heavy hole and light hole bands can be obtained using the following equation:

$$m_{hh}^{*3/2} = m_{hh}^{*3/2} + m_{lh}^{*3/2} \quad (S5)$$

where  $m_{hh}^*$  and  $m_{lh}^*$  is the effective mass of the heavy hole and light hole band, respectively.

## B. Computing lattice thermal conductivity

### 1. *thirdorder.py* supercell size

The *thirdorder.py* script is part of the ShengBTE suite. It computes the anharmonicity of the system using the finite-displacement supercell approach. The size of the supercell in the *thirdorder.py* set (containing 332 jobs) corresponded to a  $2 \times 2 \times 2$  cubic supercell containing 96 atoms. The interactions up to the third nearest neighbour were computed, which corresponds to a cut-off radius  $R_c = 0.545$  nm. Due to the finite-displacement direct approach, the shape of the supercell should be as near-cubic as possible, in order to optimise the supercell size: $R_c$  ratio and hence achieve the best possible force constants convergence with the least amount of simulated particles. Thus, a cubic unit cell, corresponding to four elementary rhombohedral cells, was used as a starting point for all phonon calculations.

In addition to the force constants, the *CONTROL* file in ShengBTE requires a few more convergence parameters to be defined. In our case, a  $9 \times 9 \times 9$  grid of planes in reciprocal space and a *scalebroad* (smearing parameter) of 1.0 were enough to converge the lattice thermal conductivity.

### 2. Adding intrinsic and extrinsic contributions to $\kappa_{latt}$

The total phonon relaxation time is in practice a combination of scattering rates of the different contributions. Therefore it is calculated using Matthiessen's rule:

$$\tau_{tot}^{-1} = \tau_{3P}^{-1} + \tau_{GB}^{-1} + \tau_{PD}^{-1} + \tau_{EP}^{-1} \quad (S6)$$

where the subscripts 3P (three-phonon processes), GB (grain boundaries), PD (point defects) and EP (electron-phonon interaction) indicate the type of interaction contributing to the final scattering rate.

The output of ShengBTE is the intrinsic lattice thermal conductivity  $\kappa_{int}$ , which only depends on  $\tau_{3P}$ . Hence all additional contributions need be included separately.

### 3. Grain boundary scattering

The relaxation time due to grain boundaries can be calculated from their size ( $L_{GB}$ ) and the velocity of the phonons ( $v$ ):

$$\tau_{GB}^{-1} = v/L_{GB} \quad (S7)$$

The ShengBTE result ( $\kappa_{int}$ ) can be approximated to be proportional to  $\tau_{3P}$  ( $\kappa_{int} \propto \text{constant} \times \tau_{3P}$ ). When the contribution of grain boundary scattering is included alongside the ShengBTE result,  $\tau_{tot}$  is calculated using  $\tau_{tot}^{-1} = \tau_{3P}^{-1} + \tau_{GB}^{-1}$ . In such case, the value of the lattice thermal conductivity with the effect of the grain boundaries ( $\kappa_{GB}$ ) can be expressed as:

$$\kappa_{GB} = \frac{\kappa_{int}}{1 + \frac{\lambda_{mfp}}{L_{GB}}} \quad (S8)$$

where  $\lambda_{mfp}$  is the mean free path of phonons. Although convenient, using a single value for  $\lambda_{mfp}$  is rather unreasonable because not all phonons travel with the same velocity, nor do they have the same relaxation time, nor the same

contribution to the total thermal conductivity ( $\kappa_{int}$ ). Instead we differentiate the ShengBTE result for total intrinsic lattice thermal conductivity with respect to  $\lambda_{mfp}$ . This gives us information on the lattice thermal conductivity ( $\kappa'_{int}$ ) of phonons with a given mean free path ( $\lambda'_{mfp}$ ). Then Eqn. S8 is applied to every value of  $\lambda'_{mfp}$  and its respective  $\kappa'_{int}$ . Then the final result is integrated back to obtain  $\kappa_{GB}$ .

#### 4. Point defects

Doping introduces point defects into the structure and the lattice thermal conductivity with point defects included ( $\kappa_{PD}$ ) can be calculated using the empirical Klemens' equation[32]:

$$\kappa_{PD} = \kappa_{GB} \left( \frac{\omega_0}{\omega_m} \right) \arctan \left( \frac{\omega_m}{\omega_0} \right) \quad (S9)$$

$$\frac{\omega_0}{\omega_m} = \sqrt{\frac{4\gamma^2 k_B T}{3\pi G_H V_a x_a} \frac{M}{\Delta M}} \quad (S10)$$

where  $\kappa_{GB}$  is the lattice thermal conductivity obtained at the previous stage (or  $\kappa_{int}$  if grain boundaries are to be neglected). The Debye and point defects frequency cut-off are given by  $\omega_m$  and  $\omega_0$ , respectively. The other parameters  $\gamma$ ,  $G_H$ ,  $V_a$  and  $x_a$  represent the Grüneisen parameter, shear modulus, volume per atom and doping concentration per atom in the unit cell. In our case  $x_a = x_d/12$  with  $x_d$  being the calculation specified doping level. The mass of the host atom (Nb or Ta) is given by  $M$ , whereas the mass difference between the host atom and the dopant atom is given by  $\Delta M$ .

#### 5. Electron-phonon interaction

The computation of the electron-phonon interaction from first-principles is expensive. However, a more empirical, but tested, approach based on the Callaway model [1, 33] can be used to gain an insight of how the electron-phonon interaction affects the lattice thermal conductivity in terms of temperature and doping concentration. The relaxation time due to electron-phonon interaction satisfies[34]:

$$\tau_{EP}^{-1} = C\omega^2 \quad (S11)$$

where  $C$  is given by[35]:

$$C = \frac{4nm^*v_e\lambda_e}{15\rho v^2} \quad (S12)$$

where  $\omega$  is the phonon frequency,  $n$  is the doping concentration,  $m^*$  is the effective mass,  $v_e$  is the electron velocity,  $\lambda_e$  is the mean free path of the electrons,  $\rho$  is the mass density, and  $v$  is the phonon velocity. In principle, the value of  $C$  can be calculated from first principles. In practice, however, the value of  $v_e$  and  $\lambda_e$  is related to the relaxation time, which is modelled to be constant with respect to doping. Therefore, estimating a parameter, which aims to show how doping affects the electron-phonon interaction, with a relaxation time, which is modelled to be insensitive to doping, would lead to a significant inaccuracy in the final results. Instead, we use the experimental results presented by He *et al.*[1] to obtain a value proportional to  $C$  at  $T = 300$  K and  $x = 0.05$ , and then we include the doping dependency ( $C \propto n_h$ ) and temperature dependency ( $C \propto T^{-1/2}$ ) to the model.

Despite the necessity of using experimental data to obtain  $C$ , this step also serves as a valuable estimate of the quality of all previous stages in modelling  $\kappa_{latt}$ . Fig. 5 shows that when all contributions are included, there is an extremely good match between experimental measurements for NbFeSb and our theoretical results.

## VI. USING ELASTIC CONSTANTS TO COMPUTE LATTICE THERMAL CONDUCTIVITY

As discussed in the manuscript, the intrinsic lattice thermal conductivity can be calculated in several ways. Here we compare the results obtained for NbFeSb and TaFeSb by solving the phonon BTE (ShengBTE) and Slack's equation. For Slack's equation, we use the approach suggested by Jia *et al.* [29], where  $\Theta_D$  and  $\gamma$  are calculated from the

Table S1. Elastic constants, bulk ( $B_H$ ) and shear ( $G_H$ ) moduli of NbFeSb and TaFeSb. The longitudinal, transverse and average phonon velocities are given by  $v_L$ ,  $v_T$ ,  $v_{av}$ , respectively. Grüneisen parameter and Debye temperature are given by  $\gamma$  and  $\Theta_D$ . Experimental results are taken from Tavassoli *et al.*, [2] where the data is obtained via Resonant Ultrasound Spectroscopy (RUS) at room temperature.

Compound	NbFeSb (this work)	NbFeSb (exp RUS [2])	TaFeSb (this work)
$c_{11}$ (GPa)	311.5	-	326.8
$c_{12}$ (GPa)	94.3	-	100.3
$c_{44}$ (GPa)	66.0	-	77.6
$B_H$ (GPa)	166.7	156	175.8
$G_H$ (GPa)	80.7	81	89.6
$v_L$ (m/s)	5 674	5 597	5 115
$v_T$ (m/s)	3 082	3 099	2 818
$v_{av}$ (m/s)	3 438	3 452	3 140
$\gamma$ [from phonon BTE]	1.76	-	1.79
$\gamma$ [from elastic moduli]	1.72	-	1.64
$\Theta_D$ (K)	393.4	394	359.5

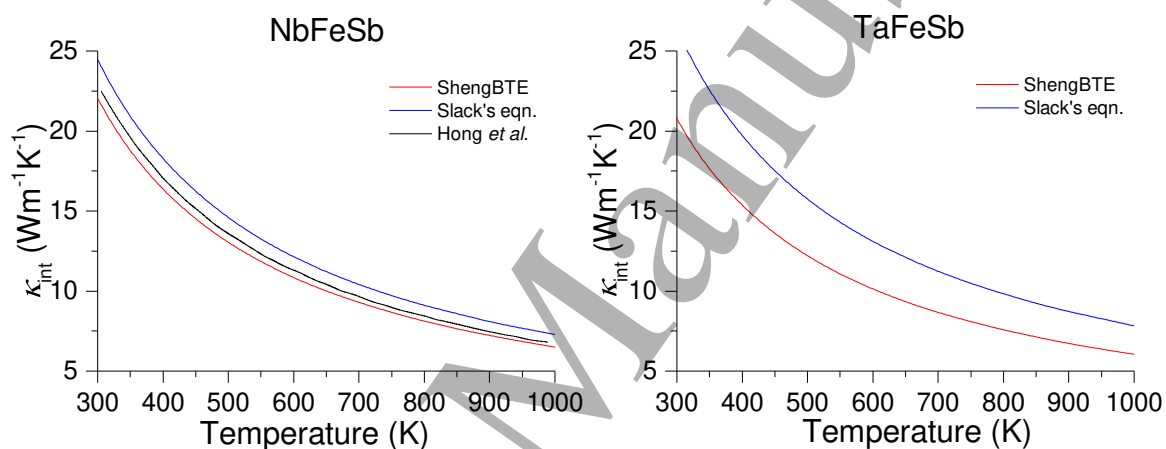


Figure S1. Comparison of the intrinsic lattice thermal conductivity of NbFeSb (left) and TaFeSb (right) when obtained by solving the phonon BTE and the Slack's equation.

bulk and shear moduli. We also compare the NbFeSb results to the one obtained by Hong *et al.*, who employed the quasi-harmonic approximation (QHA) to calculate  $\Theta_D$  and  $\gamma$  before solving Slack's equation. In terms of speed, Jia *et al.* approach is the fastest one, followed by QHA method, while the phonon BTE remains last.

Figure S1 shows that all tested methods yield relatively close results for NbFeSb, with the largest difference between the values of  $\kappa_{int}$  being 11% at room temperature. The TaFeSb results, however, show a difference up to 27% at room temperature, which will have a noticeable impact on the rest of the  $ZT$  calculations. Our analysis suggests the larger discrepancy in the TaFeSb results is mainly due to the different Grüneisen parameter (a measure of the anharmonicity of the system) obtained using ShengBTE or the elastic moduli, as shown in Table S1. Therefore, it can be concluded that Slack's equation offers a rather inexpensive way of calculating the lattice thermal conductivity of NbFeSb, but a more sophisticated approach, like the phonon BTE, is required to calculate accurately the anharmonicity and the lattice thermal conductivity of TaFeSb.

The mathematical formulae needed to follow the Jia *et al.* [29] approach are presented below. The intrinsic lattice thermal conductivity can be calculated via the bulk and shear moduli of the material using Slack's equation[28]:

$$\kappa_{int} = A \frac{\Theta_D^3 V_a^{1/3} m_{av}}{\gamma^2 n^{2/3} T} \quad (S13)$$

where  $\Theta_D$ ,  $V_a$ ,  $m_{av}$ ,  $\gamma$  and  $n$  are the Debye temperature, the volume per atom (in Å), the average atomic mass (in amu), the Grüneisen parameter and the number of atoms in the unit cell, respectively. The parameter  $A$  is given by the following equation:

$$A = \frac{2.43 \times 10^{-6}}{1 - \frac{0.514}{\gamma} + \frac{0.228}{\gamma^2}} \quad (\text{S14})$$

The averaged sound velocity  $v_{\text{av}}$  can be calculated from the velocities of the longitude  $v_L$  and shear  $v_T$ :

$$v_L = \sqrt{\frac{B_H + (4/3)G_H}{\rho}}, \quad v_T = \sqrt{\frac{G_H}{\rho}}, \quad v_{\text{av}} = \left[ \frac{1}{3} \left( \frac{1}{v_L^3} + \frac{2}{v_T^3} \right) \right]^{-\frac{1}{3}}. \quad (\text{S15})$$

where  $B_H$ ,  $G_H$  and  $\rho$  are the bulk modulus, shear modulus and the density of the compound, respectively. The Debye temperature  $\Theta_D$  can be calculated using the sound velocity::

$$\Theta_D = \frac{\hbar}{k_B} v_{\text{av}} \left( \frac{6\pi^2 n}{V_a} \right)^{\frac{1}{3}} \quad (\text{S16})$$

where  $\hbar$  and  $k_B$  are the reduced Planck's constant and Boltzmann constant.

The only remaining parameter needed for the calculation of  $\kappa_{\text{int}}$  is the Grüneisen parameter  $\gamma$  and it can be obtained from the Poisson ratio  $\nu$  in the following way:

$$\gamma = \frac{3}{2} \left( \frac{1 + \nu}{2 - 3\nu} \right), \quad \nu = \frac{1 - 2(v_T/v_L)^2}{2 - 2(v_T/v_L)^2}. \quad (\text{S17})$$

## VII. FORMATION ENERGY

The formation energy of NbFeSb and TaFeSb in Table S2 show that the crystal structure of both compounds is energetically stable, as expected from experimental results. This complements the observation of mechanical stability as seen in the phonon calculations.

Table S2. Formation energy of NbFeSb and TaFeSb.

Compound	Space group	Total energy (eV)	
Nb (1 atom/unit cell)	229	-1656.6056	
Ta (1 atom/unit cell)	229	-8434.1596	
Fe (1 atom/unit cell)	229	-862.9631	
Sb (2 atoms/unit cell)	166	-4769.5524	
			Formation energy/atom (eV/atom)
NbFeSb (3 atoms/unit cell)	216	-4905.4042	-0.3531
TaFeSb (3 atoms/unit cell)	216	-11682.7633	-0.2881